



Ternary manganese ferrite/graphene/polyaniline nanostructure with enhanced electrochemical capacitance performance

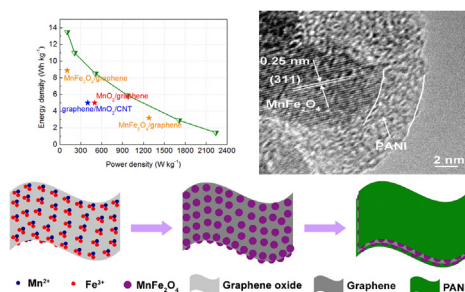
Pan Xiong, Chenyao Hu, Ye Fan, Wenyao Zhang, Junwu Zhu*, Xin Wang*

Key Laboratory for Soft Chemistry and Functional Materials of Ministry Education, Nanjing University of Science and Technology, Nanjing, China

HIGHLIGHTS

- A ternary manganese ferrite/graphene/polyaniline nanostructure is designed and synthesized.
- The ternary nanostructure shows the highest performance among all studied electrodes.
- The assembled symmetric supercapacitor exhibits a maximum energy density of 13.5 W h kg^{-1} .

GRAPHICAL ABSTRACT



ARTICLE INFO

Article history:

Received 27 February 2014

Received in revised form

7 May 2014

Accepted 7 May 2014

Available online 21 May 2014

Keywords:

Manganese ferrite

Graphene

Polyaniline

Ternary nanostructure

Supercapacitor

ABSTRACT

A ternary manganese ferrite/graphene/polyaniline (MGP) nanostructure is designed and synthesized via a facile two-step approach. This nanostructure exhibits outstanding electrochemical performances, such as high specific capacitance (454.8 F g^{-1} at 0.2 A g^{-1}), excellent rate capability (75.8% capacity retention at 5 A g^{-1}), and good cycling stability (76.4% capacity retention after 5000 cycles at 2 A g^{-1}), which are superior to those of its individual components (manganese ferrite, reduced-graphene oxide, polyaniline) and corresponding binary hybrids (manganese ferrite/graphene (MG), manganese ferrite/polyaniline (MP), and graphene/polyaniline (GP)). A symmetric supercapacitor device using the as-obtained hybrid has been fabricated and tested. The device exhibits a high specific capacitance of 307.2 F g^{-1} at 0.1 A g^{-1} with a maximum energy density of 13.5 W h kg^{-1} . The high electrochemical performance of ternary MGP can be attributed to its well-designed nanostructure and the synergistic effect of the individual components.

© 2014 Elsevier B.V. All rights reserved.

1. Introduction

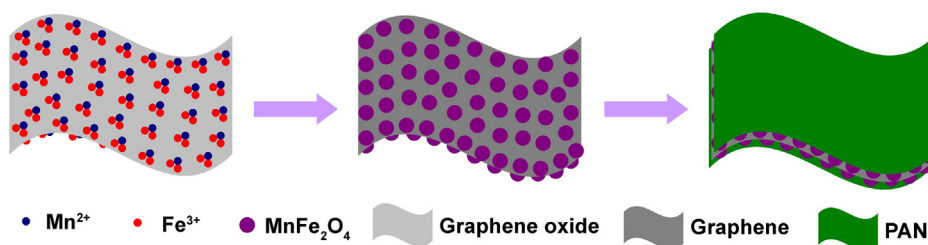
The ever-increasing energy demand and ever-worsening global environmental issues call for not only urgent development of alternatively renewable energy sources, but also more advanced energy storage and management devices. As intermediate systems between batteries and traditional dielectric capacitors,

supercapacitors exhibit the desirable properties, e.g. high power density, long cycle life ($>100,000$ cycles), and rapid charging/discharging rates, thus they are probably one of the most important next-generation energy storage devices [1–3].

It is well known that transition metal oxides possess multiple oxidation states/structures that enable rich redox reactions for pseudocapacitance generation [4]. Among the transition metal oxides, RuO_2 is one of the most prominent materials due to its ultrahigh pseudocapacitance. Even though, the extraordinarily high cost has greatly limited its commercial applications. Therefore, exploration of alternative and inexpensive electrode materials with

* Corresponding authors. Tel.: +86 25 84305667; fax: +86 25 8431 5054.

E-mail addresses: wangx@njust.edu.cn, zhujw@njust.edu.cn (X. Wang).



Scheme 1. Schematic illustration for the formation of ternary manganese ferrite/graphene/polyaniline (MGP) nanostructure.

high performance has been one of the most active research areas in supercapacitor electrode materials [5,6]. Many efforts have been paid to inexpensive metal oxides, such as oxides of Mn [7,8], Ni [9], Co [10], Fe [11,12], and so forth owing to their low cost, and environmental compatibility. Unfortunately, these simple metal oxides exhibit low specific capacitance, particularly at higher charge/discharge rates. It is of great interest to design complex metal oxide-based systems having high specific capacitance and low cost. If that can be accomplished, then it should be possible to obtain much more effective and cheaper supercapacitors.

Spinel ferrites (MFe_2O_4 , $\text{M} = \text{Fe, Co, Ni, Cu, Mn}$) have been conceived as a promising cost-effective and scalable alternative for supercapacitors due to their greater electronic conductivity and electrochemical activity than single component metal oxides [13–18]. Zhu et al. reported CuFe_2O_4 nanospheres with hierarchically porous structure, which can be used as an excellent electrode material in supercapacitor with high specific capacitance and good retention [16]. As another important member of ferrite family, manganese ferrite (MnFe_2O_4) has been widely used in microwave and magnetic recording application [19], electrocatalytic oxygen evolution reaction [20], thermochemical water splitting [21], and so on. However, relatively little attention has been paid to the electrochemical properties of MnFe_2O_4 . Recently, Kuo et al. reported the electrochemical capacitance of MnFe_2O_4 in aqueous electrolyte [17]. Nevertheless, it is noted that the pure MnFe_2O_4 only exhibited an average capacitance of about 100 F g^{-1} . A prospective way to enhance the electrochemical performance is designing novel MnFe_2O_4 -based hybrids.

Over the past decades, p-conjugated materials, such as conducting polymer, carbon nanotubes and graphene sheets, have emerged as important players in the development of new generations of energy storage and conversion devices [22–24]. Although polyaniline (PANI) itself possesses low cost, large pseudo-capacitance, and fast doping/de-doping rate, its poor cycling stability is a fatal shortcoming [25]. Graphene, a single layer of graphite, is becoming a very promising nanomaterial due to its unique electronic, optical, thermal, and mechanical properties. However, graphene sheets have a high tendency to restack themselves, and large scale production of highly qualified graphene still remains essentially unresolved [26,27]. Recently, ternary hierarchical systems composed of carbon nanomaterials, conducting polymers and transition metal oxides have been explored. These novel ternary hybrids exhibited much higher specific capacitance than the individual components or the binary carbon nanomaterials (or conducting polymers)/transition metal oxides composites [28–36]. Most recently, our group reported a ternary CoFe_2O_4 /graphene/PANI nanocomposite as a supercapacitor electrode material. Such a ternary composite can fully utilize superiority of each component, leading to the highest specific capacitance among all the electrode materials studied [37]. Although MnFe_2O_4 and CoFe_2O_4 all have a spinel structure, they differ in the distribution of the cations among the octahedral and tetrahedral sites in

the structure. Particularly, MnFe_2O_4 itself was found to exhibit larger capacitance than the other ferrites, such as Fe_3O_4 , CoFe_2O_4 , and NiFe_2O_4 [38]. Therefore, it is interesting to design novel ternary MnFe_2O_4 /carbon nanomaterials/conducting polymers composites, which may exhibit enhanced electrochemical capacitance performance compared with its individual components. To the best of our knowledge, very few studies on the synthesis of MnFe_2O_4 -based hybrids have been reported so far, especially this intriguing ternary nanostructure.

In this work, we have successfully designed and synthesized the ternary manganese ferrite/graphene/polyaniline (MGP) hybrid through a facile two-step strategy (Scheme 1). The MnFe_2O_4 nanoparticles are well dispersed on the surfaces of graphene sheets via a hydrothermal reaction because the negatively charged oxygen-containing groups of graphene oxide (GO) undergo chemical interactions with the positively charged metal ions [39]. Then a subsequent in-situ polymerization strategy is adopted for coating with polyaniline. There is also interaction between MnFe_2O_4 nanoparticles and polyaniline (PANI) because the nitrogen atoms of PAN can bond to the metal ions of MnFe_2O_4 through their lone pairs [40]. Thus this stable sandwich structure is expected to have enhanced electrochemical capacitance and improved cycling stability than the individual components or the corresponding binary hybrids.

2. Experimental section

2.1. Synthesis of ternary MnFe_2O_4 /graphene/PANI (MGP)

Graphite oxide (GO) was prepared from purified natural graphite bought from Shanghai Yifan Company with a mean particle size of $1.5 \mu\text{m}$ by a modified Hummers method as described previously [41]. Binary MnFe_2O_4 /graphene (MG) was prepared by a hydrothermal method [42]. Graphite oxide (50 mg), $\text{MnCl}_2 \cdot 4\text{H}_2\text{O}$ (0.65 mmol), and $\text{FeCl}_3 \cdot 6\text{H}_2\text{O}$ (1.30 mmol) were well dispersed and mixed together in 70 mL of ethylene glycol. A stable homogeneous emulsion was obtained after adjusting pH to 10 with NaOH solution. The resulting mixture was transferred into a 100 mL Teflon-lined stainless steel autoclave and heated to 180°C for 24 h. The precipitate was filtered, washed with ethanol and distilled water, and dried in a vacuum oven at 60°C . For comparison, the pure MnFe_2O_4 was prepared via a similar procedure without the addition of graphite oxide, and the reduced-graphene oxide (rGO) were also prepared via the similar procedure without the addition of $\text{MnCl}_2 \cdot 4\text{H}_2\text{O}$ and $\text{FeCl}_3 \cdot 6\text{H}_2\text{O}$.

Ternary MGP was synthesized via in situ polymerization of aniline monomers in the presence of binary MG [37]. 400 mg of MG and ammonium peroxydisulfate (APS, 0.75 g) were dispersed in 100 mL of 0.1 mol L^{-1} *p*-toluene sulfonic acid aqueous solution with ultrasonic vibrations for 30 min to obtain a uniform suspension. Aniline (0.3 mL) was added into this mixture dropwise under vigorous stirring in an ice-water bath, after which, the resulting

mixture was allowed to polymerize under stirring for 24 h in the ice-water bath. Finally the ternary MGP hybrid was filtered out and washed with a large amount of deionized water. The PANI were prepared without the addition of binary MG. The binary $\text{MnFe}_2\text{O}_4/\text{PANI}$ (MP) composites were synthesized via a similar procedure by replacing binary MG with pure MnFe_2O_4 . The binary graphene/PANI (GP) hybrids were prepared via a similar process in the presence of rGO instead of binary MG.

2.2. Characterization

X-ray diffraction (XRD) patterns were performed on a Bruker D8 Advance diffractometer with $\text{Cu K}\alpha$ radiation ($\lambda = 1.5406 \text{ \AA}$) and the diffraction data were recorded for 2θ angles between 5° and 80° . Raman spectra were acquired on a LabRAM ARAMIS Raman microprobe using an excitation wavelength of 532 nm. Transmission electron microscopy (TEM) and high-resolution transmission electron microscopy (HRTEM) measurements were performed by a JEOL JEM2100 transmission electron microscope. XPS measurements were performed on a Thermo ESCALAB250 spectrometer using a monochromatized Al $\text{K}\alpha$ X-ray source (1486.6 eV). The TG analyses were carried out in a TGA/SDTA851e thermogravimetric analyzer under an air atmosphere from 50 to 700°C at a heating rate of $10^\circ\text{C min}^{-1}$.

2.3. Electrochemical measurements

The working electrodes were prepared by thoroughly mixing the as-prepared composites, acetylene black, and polytetrafluoroethylene (1% wt) with the mass ratio 80:15:5 to obtain a homogeneous slurry. The slurry was coated and pressed onto nickel foam and dried under vacuum at 60°C for 24 h. In a three-electrode system, 1 M KOH was used as the electrolyte, platinum foil and Hg/HgO electrodes were used as the counter and reference electrodes, respectively. In a two-electrode system, the test capacitor were fabricated by sandwiching a filter paper soaked with 1 M KOH between two working electrodes. Two Pt foils were used as the current collectors. All the components were assembled into a layered structure and sandwiched between two PTFE sheets [37]. Cyclic voltammetry (CV) and electrochemical impedance spectroscopy (EIS) were performed by a CHI 760C workstation. EIS was recorded under the following conditions: AC voltage amplitude 5 mV, frequency range 10^5 –0.01 Hz. Galvanostatic charge/discharge testing was performed by a Land Battery workstation.

3. Result and discussion

3.1. Characterization of ternary $\text{MnFe}_2\text{O}_4/\text{graphene}/\text{PANI}$ (MGP)

The XRD diffraction patterns of MnFe_2O_4 , binary MG, and ternary MGP are shown in Fig. 1. It can be clearly seen that all the diffraction peaks of MnFe_2O_4 can be assigned to the spinel-type structure of MnFe_2O_4 (JCPDS 73-1964). The peaks at the 2θ values of 18.1, 30.1, 35.4, 42.7, 53.5, 56.3, and 62.4° can be indexed as the (111), (220), (311), (400), (422), (511), and (440) crystal planes of MnFe_2O_4 , respectively. It is obvious that the diffraction peaks of MnFe_2O_4 are also clearly observed in the XRD patterns of binary MG. However, no typical diffraction peak of graphite oxide or reduced graphene oxide (Fig. S1) is observable, indicating that the GO or rGO was fully exfoliated in the composite [42]. For ternary MGP, the broad diffraction peak at about 25° matches with the XRD of amorphous polyaniline (Fig. S1). The characteristic diffraction peaks of both MnFe_2O_4 and PANI can be observed together. The XRD diffraction patterns of binary MP and binary GP are shown in

Fig. S1, where a broad diffraction peak of PANI is observed for binary GP, while the diffraction peaks of both MnFe_2O_4 and PANI can be observed for binary MP. Raman spectra of MnFe_2O_4 , binary MG, and ternary MGP are shown in Fig. S2. The presence of the band below 1000 cm^{-1} is ascribed to MnFe_2O_4 [43], which can be observed in both binary MG and ternary MGP.

As can be seen in Fig. 2a, the almost transparent graphene sheets are fully exfoliated and decorated homogeneously with MnFe_2O_4 nanocrystals with an average diameter of 8.5 nm (see the inset of Fig. 2a). It can also be seen that the lattice fringe spacing is 0.25 nm, corresponding to the (311) planes of MnFe_2O_4 (Fig. 2b). The EDS image of binary MG clearly reveals the presence of C, O, Mn, and Fe elements (Fig. 2c) in the sample. The TEM image of ternary MGP nanocomposite is displayed in Fig. 2d. After in situ polymerization of aniline, the binary MG nanosheets are evenly coated by the polymer matrix. The morphology of ternary MGP are further observed using HRTEM (Fig. 2e), where a PANI layer with a thickness of about 4 nm and the MnFe_2O_4 nanoparticles with the lattice fringe spacing of 0.25 nm are clearly observed in the ternary hybrid. While the EDS result of MGP (Fig. 2f) shows that there are six elements, C, N, O, S, Mn, and Fe, confirming the existence of PANI and MnFe_2O_4 in the sample (the S signals come from the doped p-toluene sulfonic acid).

The XPS survey of ternary MGP is shown in Fig. 3a, further revealing the co-existence of C, N, O, S, Mn and Fe in the ternary MGP. The Mn/Fe atomic ratio of 1/2.16 is close to the theoretical value for MnFe_2O_4 . Mn 2p and Fe 2p spectra of ternary MGP are shown in Fig. S3a and b, respectively. The C 1s spectra of GO and MGP are shown in Fig. 3b. The C 1s spectrum of GO can be deconvoluted into four peak components with binding energies at 284.6, 286.7, 287.8, and 289.0 eV corresponding to the $\text{C}=\text{C}$, $\text{C}-\text{O}$, $\text{C}=\text{O}$, and $\text{O}-\text{C}=\text{O}$ species, respectively. While in the decomposed C 1s spectrum of ternary MGP, an additional peak at around 285.5 eV can be observed, which can be assigned to $\text{C}-\text{N}$, confirming the presence of PANI in the ternary MGP. Besides, the much weaker intensities of the oxygenated carbon can be ascribed to the reduction of graphene oxide during the hydrothermal reaction. A comparison of N 1s spectra of PANI and ternary MGP is shown in Fig. 3c. The N 1s spectrum of PANI can be deconvoluted into three distinct curves with the peaks locating at 398.9, 400.1 and 402.0 eV, respectively. The peak appearing at 398.9 eV is associated with $-\text{N}=\text{}$, the peak at 400.1 eV may be assigned to $-\text{NH}-$, and the high binding energy at 402.0 eV is due to the interaction between N^+

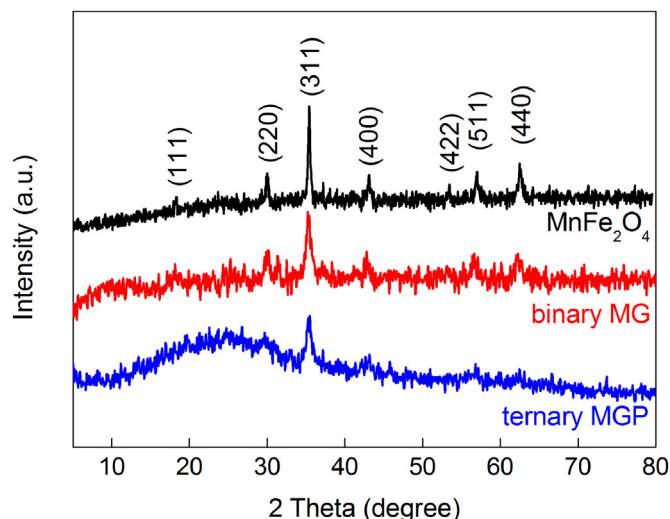


Fig. 1. The XRD patterns of MnFe_2O_4 , binary MG, and ternary MGP.

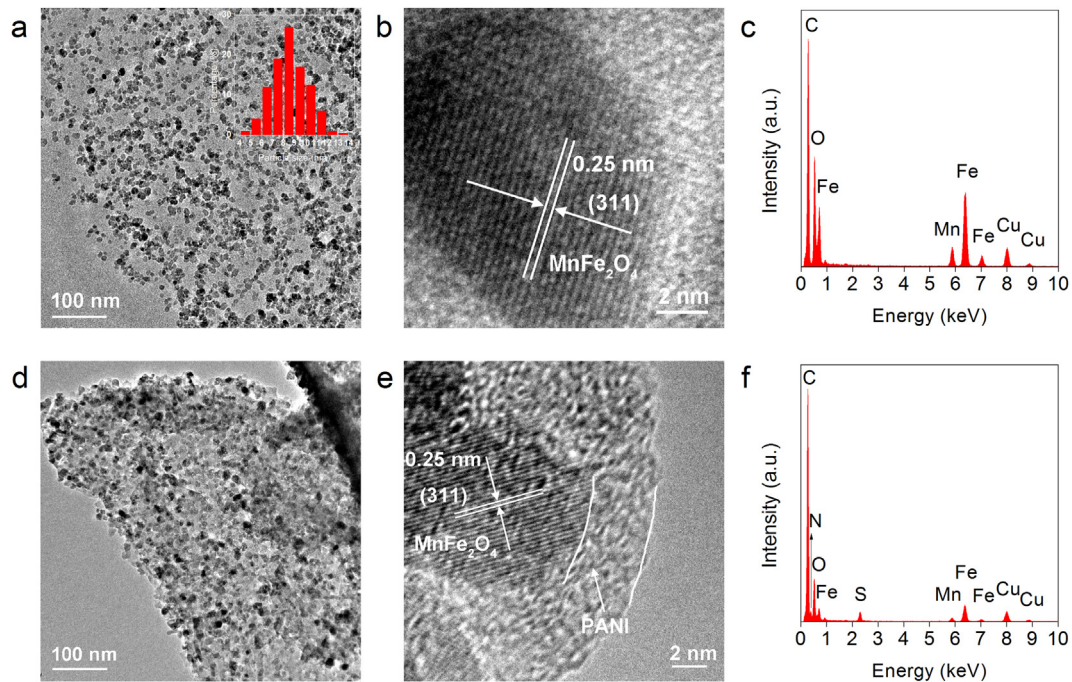


Fig. 2. (a) TEM, (b) HRTEM, and (c) EDS images of binary MG. The inset of (a) shows the particle size distribution of MnFe_2O_4 in binary MG. (d) TEM, (e) HRTEM, and (f) EDS images of ternary MGP.

and protons introduced by the acid dopant [44]. However, in the decomposed N 1s spectrum of ternary MGP, an additional peak at 399.5 eV can be observed, which may result from the interaction between nitrogen and metal ions [40,45,46].

The TG curves of the binary MG and ternary MGP nanocomposite are shown in Fig. 3d. A slight weight loss below 200 °C is due to the physically adsorbed water of the composite. The remarkable weight loss in the range of 200–540 °C corresponds to

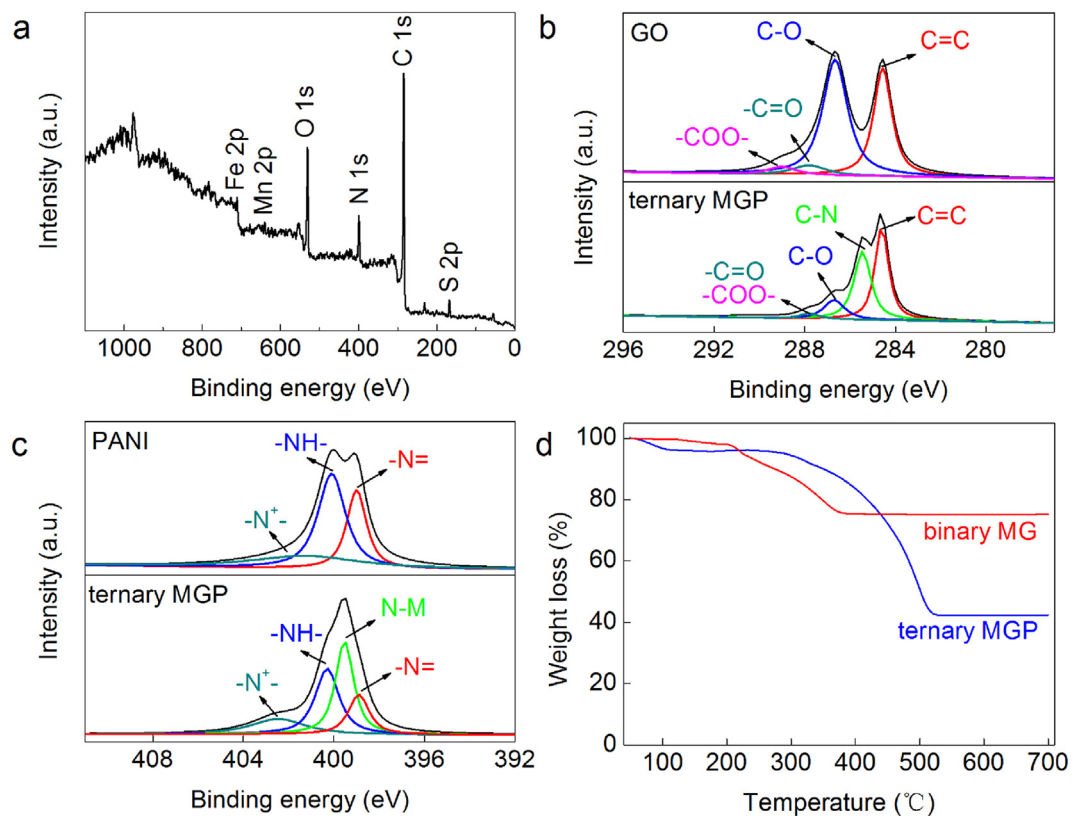


Fig. 3. (a) Survey XPS spectrum of ternary MGP, (b) C 1s spectra of GO and ternary MGP, (c) N 1s spectra of PANI and ternary MGP, (d) TG analysis of binary MG and ternary MGP.

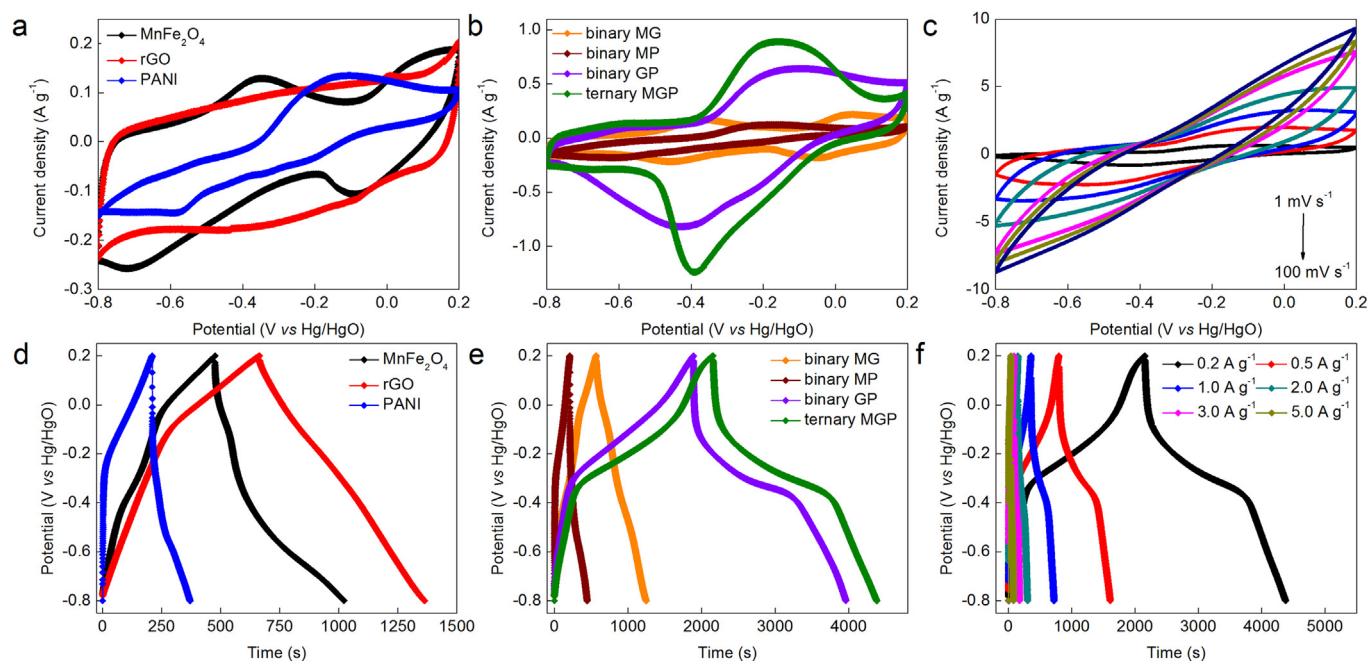
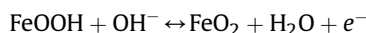
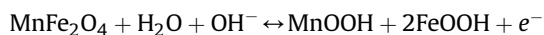


Fig. 4. Electrochemical performances of all studied electrodes in a three-electrode system: CV curves of (a) MnFe_2O_4 , rGO, and PANI, (b) binary MG, MP, GP, and ternary MGP at 1 mV s^{-1} , (c) CV curves of ternary MGP at different scan rates. Galvanostatic charge/discharge curves of (d) MnFe_2O_4 , rGO, and PANI, (e) binary MG, MP, GP, and ternary MGP at 0.2 A g^{-1} , (f) Galvanostatic charge/discharge curves of ternary MGP at different current densities.

the removal of doping anions from the polyaniline structure and degradation of the polyaniline chain and graphene [47]. For binary MG, the residue weight was about 75.3% which can be ascribed to the remaining MnFe_2O_4 and the mass ratio of MnFe_2O_4 /graphene in binary MG can be estimated to about 3/1. No noticeable change was observed above 540°C and the residue weight was about 42.3%, which can be ascribed to the remaining MnFe_2O_4 in ternary MGP. Thus the contents of graphene and PANI were estimated to be about 14.1% and 43.6%, respectively.

3.2. Electrochemical performance of ternary MnFe_2O_4 /graphene/PANI (MGP)

To evaluate the electrochemical performance of the as-obtained ternary MGP composites, cyclic voltammetry (CV) and galvanostatic charge/discharge measurements in a 1 M KOH aqueous solution using a three electrode system were carried out. CV curves of three separated components are shown in Fig. 4a. Two pairs of redox peaks indicate the pseudocapacitance behavior of MnFe_2O_4 . The redox process may be described as follows [16,17]:



rGO exhibits a nearly rectangular shape with no obvious peaks for oxidation and reduction, indicating a characteristic of the electric double-layer capacitance behavior of carbon-based materials, while PANI clearly shows a pair of redox peaks due to the redox transition between a semiconducting state (leucoemeraldine form) and a conducting state (polaronic emeraldine form) [48]. Fig. 4b presents the CV curves of binary MG, MP, GP, and ternary MGP nanocomposites. After loading MnFe_2O_4 onto rGO nanosheets, two pairs of redox peaks are observed in the CV curve of binary MG, which are ascribed to the Faradic process of MnFe_2O_4 . A pair of redox peaks is shown in the CV curves of both binary GP and

ternary MGP. Moreover, the ternary MGP nanocomposite shows the highest current density among all the electrodes, implying its best capacitive performance. Fig. 4c shows the CV curves of ternary MGP at different scan rates. It is noted that the total peak current density of ternary MGP increases obviously with increasing potential scan rate, demonstrating its good rate property and excellent capacitance behavior.

As can be seen in Fig. 4d, rGO exhibits an almost triangular shaped charge/discharge curve, implying that its capacitance is mainly attributed to pure electric double layer. However, the charge/discharge curves of both PANI and MnFe_2O_4 show deviations from linearity, which is typical of a pseudocapacitive contribution. As can be seen in Fig. 4e, among binary MG, MP, GP, and ternary MGP, the MGP exhibits the longest discharge time, indicating the highest electrochemical performance. As shown in Fig. 4f, all charge/discharge curves still exhibit a similar shape with the increase of current densities, revealing the ideal capacitive behaviors of the ternary MGP nanocomposite. The specific capacitances at different current densities can be calculated by the following equation:

$$C_s = \frac{i \times \Delta t}{\Delta V} \quad (1)$$

where C_s is the specific discharge capacitance in F g^{-1} , i is the current density in A g^{-1} , Δt is the discharge time in s, and ΔV is potential drop during discharge. The results of binary MG, MP, GP, and ternary MGP are plotted together in Fig. 5a. Encouragingly, the ternary MGP shows high specific capacitance of 454.8, 425.2, 400.7, 365.6, 354.7, and 344.7 F g^{-1} at 0.2, 0.5, 1, 2, 3, and 5 A g^{-1} , respectively. It is worth noting that, MGP still maintained a specific capacitance as high as 344.7 F g^{-1} at 5 A g^{-1} , while the specific capacitance of binary GP decreased rapidly to 134.5 F g^{-1} at the same current density. The retention rates of the specific capacitance for binary MG, MP, GP, and ternary MGP are 62.6%, 5.51%, 31.8%, and 75.8%, respectively. These results illustrate the high capacity at a

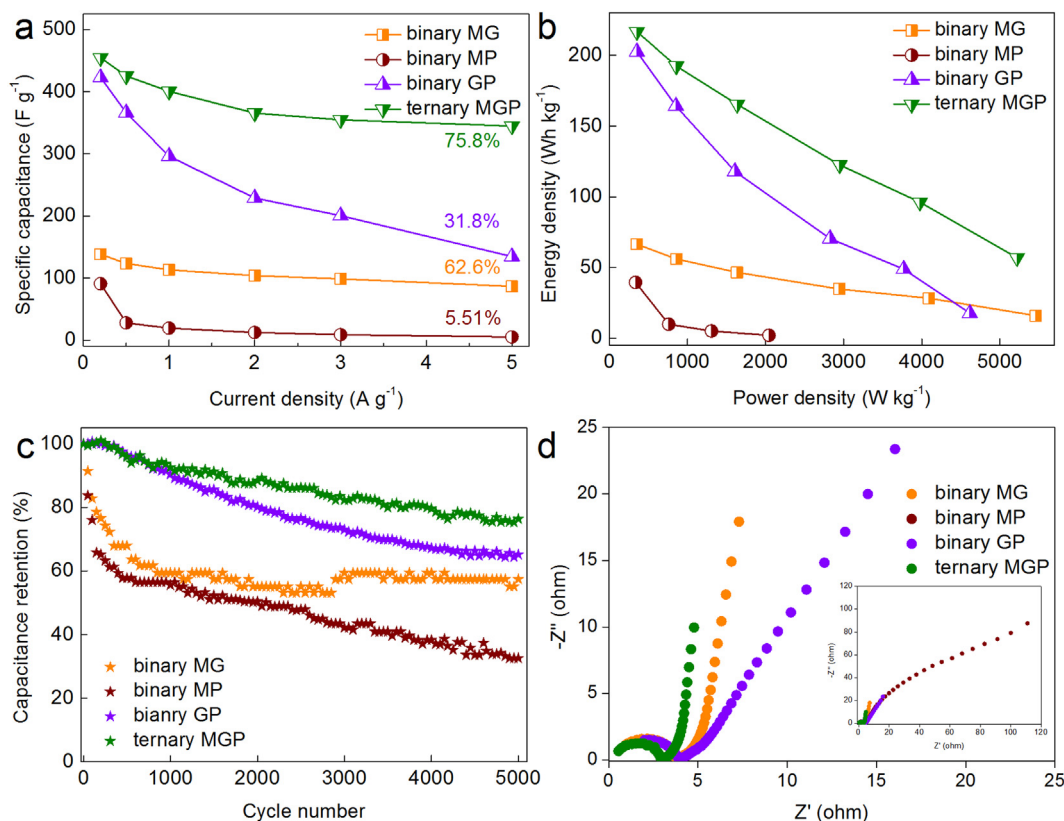


Fig. 5. (a) Variations of the specific capacitance with current density for binary MG, MP, GP and ternary MGP. (b) Ragone plots of binary MG, MP, GP, and ternary MGP calculated from galvanostatic charge/discharge curves. (c) Cycle stability of binary MG, MP, GP, and ternary MGP during the long-term charge/discharge process at a current density of $2 A g^{-1}$. (d) EIS measurement of binary MG, binary MP, binary GP, and ternary MGP.

wide range of current densities, and terrific rate capability of the ternary MGP.

The energy density ($E, Wh kg^{-1}$) and power density ($P, W kg^{-1}$) can be calculated from charge/discharge curves using Equations (2) and (3), respectively.

$$E = \frac{1}{2} C_s (\Delta V)^2 \quad (2)$$

$$P = \frac{E}{\Delta t} \quad (3)$$

As can be seen from Fig. 5b, the ternary MGP electrode exhibits much higher capacitive performance than that of binary MG, MP, or GP. Remarkably, a high energy density of $216.74 Wh kg^{-1}$ at a power density of $351.47 W kg^{-1}$ was attained with ternary MGP, in contrast, binary MG, MP, and GP showed lower values of 66.52, 39.45, and $202.57 Wh kg^{-1}$, respectively. In addition, ternary MGP still maintained an energy density of $56.97 Wh kg^{-1}$ even when the power density increased to $5218 W kg^{-1}$. The long-term cycling performance of binary MG, MP, GP, and ternary MGP are plotted together in Fig. 5c, where it can be seen that about 77% of the specific capacitance of the ternary MGP can be retained after 5000 cycles, demonstrating its highest cycling stability among all the electrodes. The Nyquist impedance plots of binary MG, MP, GP, and ternary MGP are shown in Fig. 5d, each of them exhibits a half semicircle in the high-frequency region, followed a line in the low-frequency region. Due to the poor electrical conductivity of PANI in KOH electrolyte, the binary MP showed the highest resistance. While after addition of well-conductive graphene, the electrical conductivities of binary MG, GP, and ternary MGP can be effectively

improved. The impedance arc is related to charge-transfer resistance (R_{ct}) at the electrode material–electrolyte interface. As compared to binary GP (2.9Ω) and MG (3.4Ω), a lower R_{ct} (2.7Ω) of ternary MGP implies that the ternary MGP has the fastest charge transfer rate among all samples tested in this study, further confirming its high performance.

The good performances of ternary MGP are also compared with our previous ternary cobalt ferrite/graphene/polyaniline (CGP) hybrid [37] (Fig. S4). Although the ternary CGP showed higher specific capacitance at low current density, the specific capacitance decreased rapidly as the current density increased. A poor capacitance retention rate of 48.5% was obtained for ternary CGP, which was much lower than that of ternary MGP (78.0%) at a current density of $3 A g^{-1}$. Even when the current density increased to $5 A g^{-1}$, the specific capacitance of the ternary MGP was still maintained at a high level (75.8%). In addition, the ternary MGP exhibited larger energy density than that of ternary CGP at higher current densities. When the current density increased to $3 A g^{-1}$, only 25.4% energy density retention was observed for ternary CGP, while for the ternary MGP, a high energy density of 44.4% was maintained, and even when the current density increased to $5 A g^{-1}$, the energy density was still at a level of 26.3%.

3.3. Electrochemical performance of symmetric supercapacitor

To further evaluate the electrochemical performance of the as-obtained ternary MGP composite, a symmetric supercapacitor has been designed and fabricated. In symmetric supercapacitor, the charge balance follows the relationship $q^+ = q^-$ (q^+ is the positive electrode charge and q^- is the negative electrode charge) [8]. The

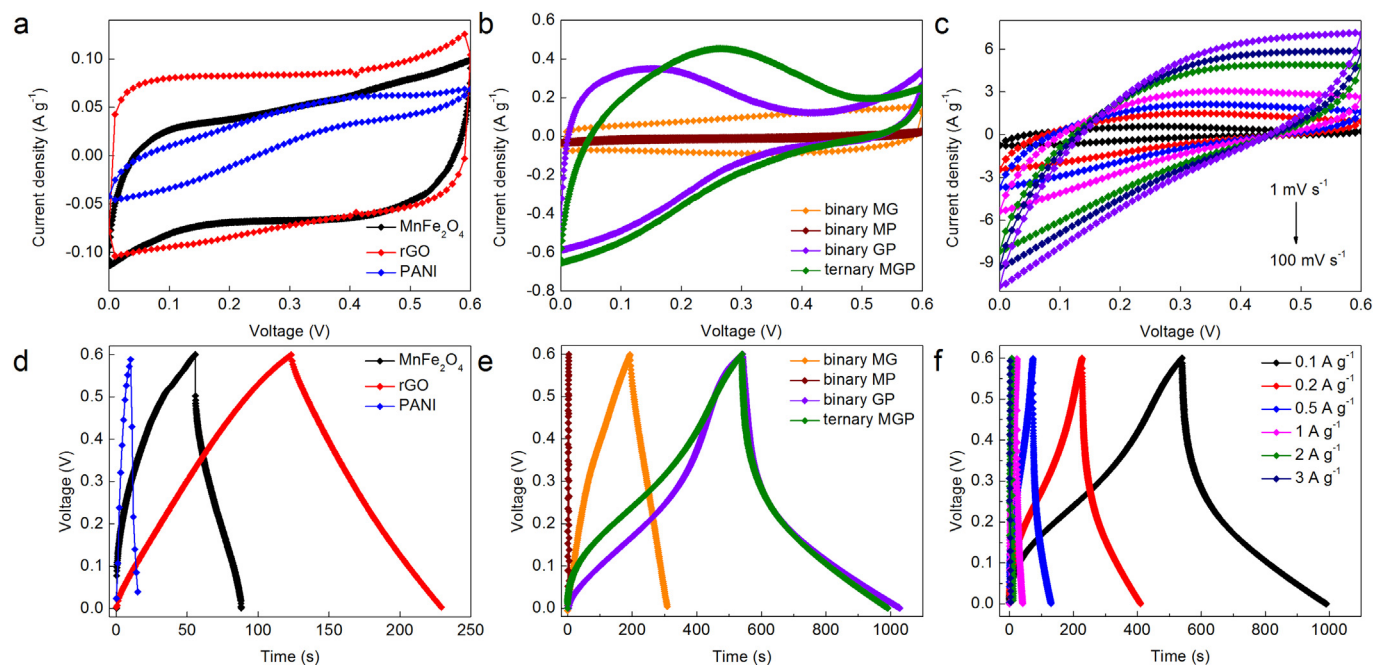


Fig. 6. Electrochemical performances of all fabricated symmetric supercapacitors: CV curves of (a) MnFe_2O_4 , rGO, and PANI, (b) binary MG, MP, GP, and ternary MGP-based symmetric supercapacitors at 1 mV s^{-1} . (c) CV curves of ternary MGP-based symmetric supercapacitor at different scan rates. Galvanostatic charge/discharge curves of (d) MnFe_2O_4 , rGO, and PANI, (e) binary MG, MP, GP, and ternary MGP-based symmetric supercapacitors at 0.2 A g^{-1} . (f) Galvanostatic charge/discharge curves of ternary MGP-based symmetric supercapacitor at different current densities.

charge stored by each electrode depends on the specific capacitance (C_s), the potential window (ΔV) during the charge/discharge process and the mass of the active materials (m) following: $q = C_s \times \Delta V \times m$, and in order to get $q^+ = q^-$, $C_s^+ \times \Delta V^+ \times m^+ = C_s^- \times \Delta V^- \times m^-$ [8]. The same active materials are used in both positive and negative electrodes, $C_s^+ = C_s^-$, $\Delta V^+ = \Delta V^-$. Accordingly, the mass of active materials in both positive and negative electrodes should be the same to get the charge balance. Fig. 6a and b shows the CV curves of MnFe_2O_4 , rGO, PANI, binary MG, MP, GP and ternary MGP-based symmetric supercapacitor, respectively. It is obvious that the ternary MGP-based symmetric supercapacitor shows the highest current density among all the supercapacitors, exhibiting its best capacitive performance. Fig. 6c shows the CV curves of ternary MGP-based symmetric supercapacitor at different scan rates, demonstrating the excellent rate capability. Fig. 6d and e shows the galvanostatic charge/discharge curves of MnFe_2O_4 , rGO, PANI, binary MG, MP, GP and ternary MGP-based symmetric supercapacitor, respectively. The longest discharge time of ternary MGP-based symmetric supercapacitor indicates the highest electrochemical capacitance. Fig. 6f shows the galvanostatic charge/discharge curves of ternary MGP symmetric supercapacitor at different current densities. The specific capacitances at different current densities can be calculated by the following equation [49],

$$C_s = \frac{4i \times \Delta t}{\Delta V} \quad (4)$$

where C_s is the capacity of one electrode for the two-electrode cell in F g^{-1} , i is the discharge current density in A g^{-1} , Δt is the discharge time in s, and ΔV is potential drop during discharge. The variations of the specific capacitance with the current density of binary MG, MP, GP and ternary MGP-based symmetric supercapacitor are plotted together in Fig. 7a. The ternary MGP-based symmetric supercapacitor shows high specific capacitance of 307.2, 253.6, 211.5, 144.6, 102.1, and 66.62 F g^{-1} at 0.1, 0.2, 0.5, 1, 2,

and 3 A g^{-1} , respectively, which is more competitive than those of the three binary composite-based symmetric supercapacitors. The long-term cycling performance of ternary MGP-based symmetric supercapacitor is shown in Fig. 7b. The capacitance retention after 2000 cycles of charge/discharge at 1 A g^{-1} is about 74%, indicating an excellent long-term stability of the symmetric supercapacitor. From the charge/discharge curves, the coulombic efficiency can be determined by the ratio of discharge and charge time. As shown in Fig. S5, the ternary MGP-based symmetric supercapacitor exhibits high coulombic efficiencies at different current densities. It is noted that the coulombic efficiency remains about 98% during the cycling process (Fig. S6). The enhanced performances of ternary MGP-based symmetric supercapacitor may be attributed to the well-designed nanostructure and combination of the superiority of each component. The addition of highly conductive graphene can not only greatly improve the electrically conductive properties of the composite, but also increase electrode/electrolyte contact area [24,50]. The ultrathin PANI layer can not only provide numerous electroactive sites for efficient Faradic redox reaction, but also restricts the dissolution and aggregation of MnFe_2O_4 with the help of the graphene matrix. Besides, the interactions between PANI molecular chains and graphene nanosheets are also beneficial for enhancing the electrochemical performance [41,51]. Moreover, the MnFe_2O_4 nanoparticles may provide Faradic processes to increase the total capacitance. The presence of MnFe_2O_4 nanoparticles on the surfaces of graphene may prevent the restacking of the graphene sheets resulting in high surface areas upon cycling.

The power density (P , W kg^{-1}) and energy density (E , Wh kg^{-1}) of symmetric supercapacitor can be calculated from charge/discharge curves using Equations (3) and (5), respectively [52].

$$E = \frac{C_s (\Delta V)^2}{8} \quad (5)$$

The ternary MGP-based symmetric supercapacitor shows a high energy density of 13.5 Wh kg^{-1} at 0.1 A g^{-1} , which is a little lower

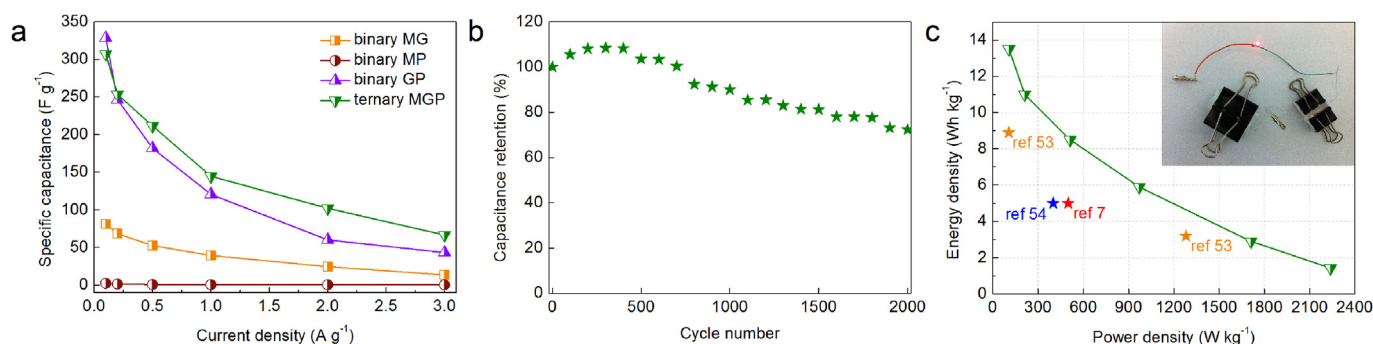


Fig. 7. (a) Variation of the specific capacitance with current density for binary MG, MP, GP and ternary MGP-based symmetric supercapacitor. (b) Cycling stability of ternary MGP-based symmetric supercapacitor at 1 A g⁻¹. (c) Ragone plots of ternary MGP-based symmetric supercapacitor compared with the values of other symmetrical systems. Inset of (c) shows the ternary MGP-based symmetric supercapacitor can light a red LED.

than that of binary GP-based symmetric supercapacitor (14.5 W h kg⁻¹), but much higher than that of binary MG-based symmetric supercapacitor (3.44 W h kg⁻¹). Moreover, ternary MGP-based symmetric supercapacitor still maintains an energy density of 1.43 W h kg⁻¹ as the power density increases to 2239 W kg⁻¹, while the energy density of binary GP-based symmetric supercapacitor is remarkably decreased to 0.453 W h kg⁻¹ at a power density of 1924 W kg⁻¹ (Fig. S7). A rough comparison shown in Fig. 7c indicates that this value is also comparable to that of majority symmetric supercapacitor devices reported in recent years such as 3D MnO₂/graphene [7], MnFe₂O₄/graphene [53], and ternary graphene/MnO₂/CNTs [54]. Finally, we assembled two symmetric supercapacitors in series to demonstrate the practical applications of the ternary MGP device, and the two symmetric supercapacitors device successfully lit a red light-emitting diode (LED) (driving voltage 1.8 V) after charging (see the inset of Fig. 7c). The volumetric energy density (E_v , W h cm⁻³) and volumetric power density (P_v , W cm⁻³) can be calculated using the following equation [55]:

$$E_v = \frac{C_v(\Delta V)^2}{8} = \frac{C_s \rho (\Delta V)^2}{8}$$

$$P_v = \frac{E_v}{\Delta t}$$

where C_v is the volumetric capacitance in F cm⁻³, ρ is the density in g cm⁻³. The Ragone plot related to E_v and P_v of binary MG, MP, GP, and ternary MGP-based symmetric supercapacitor is shown in Fig. S8, where ternary MGP exhibited the best performances. Besides, the performances of ternary MGP without binder and conductive additive are shown in Fig. S9, which exhibited an energy density of 8.7 W h kg⁻¹ at a power density of 102 W kg⁻¹.

4. Conclusions

In summary, we have successfully designed and fabricated a ternary manganese ferrite/graphene/polyaniline (MGP) nanostructure via a facile two-step strategy. This nanostructure exhibits much higher specific capacitance, highly improved rate capability and cycling stability, significantly outperforming the individual components (MnFe₂O₄, rGO and PANI) and their corresponding binary hybrids (MG, MP and GP). A symmetric supercapacitor device based on the ternary MGP has been fabricated and tested. The device shows a high specific capacitance of 307.2 F g⁻¹ at 0.1 A g⁻¹ with a maximum energy density of 13.5 W h kg⁻¹. The addition of graphene nanosheets as the conducting frameworks for sustaining MnFe₂O₄ and PANI, may not only improve the electrical

conductivity of the ternary composite, but also increase electrode/electrolyte contact area. The conducting polymer coating may provide numerous electroactive sites for efficient Faradic redox reaction and restrict the dissolution and aggregation of MnFe₂O₄. MnFe₂O₄ nanoparticles may prevent the restacking of graphene nanosheets, maintaining high surface areas during charge/discharge process. These inspiring performances would make this novel ternary nanostructure suitable for the future energy storage systems.

Acknowledgment

This work was supported by NSAF (No. U1230125), the National High Technology Research and Development Program of China (No. 2013AA050905), RFDP (No. 20123219130003), NNSF of China (No. 51322212), the Fundamental Research Funds for the Central Universities (No. 30920130122002, No. 30920130122003) and PAPD of Jiangsu.

Appendix A. Supplementary data

Supplementary data related to this article can be found at <http://dx.doi.org/10.1016/j.jpowsour.2014.05.048>.

References

- [1] P. Simon, Y. Gogotsi, *Nat. Mater.* 7 (2008) 845.
- [2] L.L. Zhang, X.S. Zhao, *Chem. Soc. Rev.* 38 (2009) 2520.
- [3] C. Liu, F. Li, L.P. Ma, H.M. Cheng, *Adv. Mater.* 22 (2010) E28.
- [4] T.Y. Wei, C.H. Chen, H.C. Chien, S.Y. Lu, C.C. Hu, *Adv. Mater.* 22 (2010) 347.
- [5] Y.T. Kim, K. Tadai, T. Mitani, *J. Mater. Chem.* 15 (2005) 4914.
- [6] Z.S. Wu, D.W. Wang, W. Ren, J. Zhao, G. Zhou, F. Li, H.M. Cheng, *Adv. Funct. Mater.* 20 (2010) 3595.
- [7] Y. He, W. Chen, X. Li, Z. Zhang, J. Fu, C. Zhao, E. Xie, *ACS Nano* 7 (2012) 174.
- [8] V. Komenko, E. Raymundo-Pinero, F. Beguin, *J. Power Sources* 153 (2006) 183.
- [9] K. Liang, X. Tang, W. Hu, *J. Mater. Chem.* 22 (2012) 11062.
- [10] X. Xia, J. Tu, Y. Mai, X. Wang, C. Gu, X. Zhao, *J. Mater. Chem.* 21 (2011) 9319.
- [11] X. Zhao, C. Johnston, P.S. Grant, *J. Mater. Chem.* 19 (2009) 8755.
- [12] K. Xie, J. Li, Y. Lai, W. Lu, Z. Zhang, Y. Liu, L. Zhou, H. Huang, *Electrochem. Commun.* 13 (2011) 657.
- [13] L. Wang, H. Ji, S. Wang, L. Kong, X. Jiang, G. Yang, *Nanoscale* 5 (2013) 3793.
- [14] D.H. Deng, H. Pang, J.M. Du, J.W. Deng, S.J. Li, J. Chen, J.S. Zhang, *Cryst. Res. Technol.* 47 (2012) 1032.
- [15] S. Anwar, K.S. Muthu, V. Ganesh, N. Lakshminarasimhan, *J. Electrochem. Soc.* 158 (2011) A976.
- [16] M. Zhu, D. Meng, C. Wang, G. Diao, *ACS Appl. Mater. Interfaces* 5 (2013) 6030.
- [17] S.L. Kuo, J.F. Lee, N.L. Wu, *J. Electrochem. Soc.* 154 (2007) A34.
- [18] S.L. Kuo, N.L. Wu, *J. Power Sources* 162 (2006) 1437.
- [19] C.R. Vestal, Z.J. Zhang, *J. Am. Chem. Soc.* 125 (2003) 9828.
- [20] R.N. Singh, J.P. Singh, H.N. Cong, P. Chartier, *Int. J. Hydrogen Energy* 31 (2006) 1372.
- [21] C. Alvani, G. Ennas, A. Barbera, G. Marongiu, F. Padella, F. Varsano, *Int. J. Hydrogen Energy* 30 (2005) 1407.

- [22] Jaidev, R.I. Jafri, A.K. Mishra, S. Ramaprabhu, *J. Mater. Chem.* 21 (2011) 17601.
- [23] H.L. Wang, Q.L. Hao, X.J. Yang, L.D. Lu, X. Wang, *Nanoscale* 2 (2010) 2164.
- [24] S. Chen, J. Zhu, X. Wu, Q. Han, X. Wang, *ACS Nano* 4 (2010) 2822.
- [25] H. Jiang, P.S. Lee, C. Li, *Energy Environ. Sci.* 6 (2013) 41.
- [26] C. Liu, Z. Yu, D. Neff, A. Zhamu, B.Z. Jang, *Nano Lett.* 10 (2010) 4863.
- [27] Y. Sun, Q. Wu, G. Shi, *Energy Environ. Sci.* 4 (2011) 1113.
- [28] Y. Hou, Y. Cheng, T. Hobson, J. Liu, *Nano Lett.* 10 (2010) 2727.
- [29] Q. Li, J. Liu, J. Zou, A. Chunder, Y. Chen, L. Zhai, *J. Power Sources* 196 (2011) 565.
- [30] X. Xia, Q. Hao, W. Lei, W. Wang, D. Sun, X. Wang, *J. Mater. Chem.* 22 (2012) 16844.
- [31] X. Xia, Q. Hao, W. Lei, W. Wang, H. Wang, X. Wang, *J. Mater. Chem.* 22 (2012) 8314.
- [32] G. Yu, L. Hu, N. Liu, H. Wang, M. Vosgueritchian, Y. Yang, Y. Cui, Z. Bao, *Nano Lett.* 11 (2011) 4438.
- [33] H. Jiang, Y. Dai, Y. Hu, W. Chen, C. Li, *ACS Sustainable Chem. Eng.* 2 (2014) 70.
- [34] G. Wang, Q. Tang, H. Bao, X. Li, G. Wang, *J. Power Sources* 241 (2013) 231.
- [35] X. Lu, F. Zhang, H. Dou, C. Yuan, S. Yang, L. Hao, L. Shen, L. Zhang, X. Zhang, *Electrochim. Acta* 69 (2012) 160.
- [36] M.Q. Zhao, Q. Zhang, J.Q. Huang, G.L. Tian, T.C. Chen, W.Z. Qian, F. Wei, *Carbon* 54 (2013) 403.
- [37] P. Xiong, H. Huang, X. Wang, *J. Power Sources* 245 (2014) 937.
- [38] S.L. Kuo, N.L. Wu, *Electrochim. Solid-State Lett.* 8 (2005) A495.
- [39] Y. Liang, Y. Li, H. Wang, J. Zhou, J. Wang, T. Regier, H. Dai, *Nat. Mater.* 10 (2011) 780.
- [40] G. Wu, C.M. Johnston, N.H. Mack, K. Artyushkova, M. Ferrandon, M. Nelson, J.S. Lezama-Pacheco, S.D. Conradson, K.L. More, D.J. Myers, P. Zelenay, *J. Mater. Chem.* 21 (2011) 11392.
- [41] H. Wang, Q. Hao, X. Yang, L. Lu, X. Wang, *ACS Appl. Mater. Interfaces* 2 (2010) 821.
- [42] Y. Fu, P. Xiong, H. Chen, X. Sun, X. Wang, *Ind. Eng. Chem. Res.* 51 (2012) 725.
- [43] J. Mohapatra, A. Mitra, D. Bahadur, M. Aslam, *CrystEngComm* 15 (2013) 524.
- [44] M. Kim, C. Lee, J. Jang, *Adv. Funct. Mater.* (2013), <http://dx.doi.org/10.1002/adfm.201303282>.
- [45] A. Morozan, P. Jegou, B. Jousset, S. Palacin, *Phys. Chem. Chem. Phys.* 13 (2011) 21600.
- [46] P. Xiong, Q. Chen, M. He, X. Sun, X. Wang, *J. Mater. Chem.* 22 (2012) 17485.
- [47] J. Wang, Y. Yang, Z.H. Huang, F. Kang, *J. Power Sources* 204 (2012) 236.
- [48] J. Yan, T. Wei, Z. Fan, W. Qian, M. Zhang, X. Shen, F. Wei, *J. Power Sources* 195 (2010) 3041.
- [49] X. Zhao, L. Zhang, S. Murali, M.D. Stoller, Q. Zhang, Y. Zhu, R.S. Ruoff, *ACS Nano* 6 (2012) 5404.
- [50] Y. Zhu, S. Murali, W. Cai, X. Li, J.W. Suk, J.R. Potts, R.S. Ruoff, *Adv. Mater.* 22 (2010) 3906.
- [51] M. Zhong, Y. Song, Y. Li, C. Ma, X. Zhai, J. Shi, Q. Guo, L. Liu, *J. Power Sources* 217 (2012) 6.
- [52] L. Li, A.R. Raji, H. Fei, Y. Yang, E.L. Samuel, J.M. Tour, *ACS Appl. Mater. Interfaces* 5 (2013) 6622.
- [53] W. Cai, T. Lai, W. Dai, J. Ye, *J. Power Sources* 255 (2014) 170.
- [54] Y. Cheng, S. Lu, H. Zhang, C.V. Varanasi, J. Liu, *Nano Lett.* 12 (2012) 4206.
- [55] X. Yang, C. Cheng, Y. Wang, L. Qiu, D. Li, *Science* 341 (2013) 534.